PAPER

Development and verification of a novel scintillator-based, imaging neutral particle analyzer in DIII-D tokamak

To cite this article: X.D. Du *et al* 2018 *Nucl. Fusion* **58** 082006

IOP Publishing | International Atomic Energy Agency Nuclear Fusion

Nucl. Fusion **58** (2018) 082006 (8pp) https://doi.org/10.1088/1741-4326/aac3a2

Development and verification of a novel scintillator-based, imaging neutral particle analyzer in DIII-D tokamak

X.D. Du[1], M.A. Van Zeeland[2], W.W. Heidbrink[1] and D. Su[2]

[1] University of California Irvine, Irvine, CA, 92697, United States of America
[2] General Atomics, PO Box 85608, San Diego, CA, 92186-5608, United States of America

E-mail: duxiaodi@fusion.gat.com

Received 16 February 2018, revised 2 May 2018
Accepted for publication 10 May 2018
Published 29 June 2018

Abstract

A compact scintillator-based imaging neutral particle analyzer (INPA) that provides energy and radially resolved measurements of confined fast ions has been designed and built in the DIII-D tokamak. The system measures charge-exchanged energetic neutrals by viewing an active neutral beam source through a 1D pinhole camera with a rear collimating slit that defines the neutral particle collection sightline and radial positions probed in the plasma. The incident neutrals are ionized by ultra-thin carbon stripping foils of 10 nm thickness with the local tokamak magnetic field acting as a magnetic spectrometer to disperse the ions onto a scintillator. The strike position on the phosphor is determined by the fast ion energy and sightline while the intensity of emitted light from the phosphor is proportional to the ion flux. Fast camera measurements of the scintillator provide 2D images of the escaping neutrals mapped to energy and radial position in the plasma. The INPA system images a broad radial range from the plasma core to edge and deuterium energies up to 80 keV, with energy resolution of ∼7.5 keV and pitch angle resolution of ∼5°. The first data obtained from the INPA demonstrates that the system has excellent signal to noise ratio and provides unprecedented details of phase space dynamics.

Keywords: energetic particles, neutral particle analyzer, tokamak

(Some figures may appear in colour only in the online journal)

1. Introduction

In magnetic confinement fusion devices, a significant number of fast neutrals can be produced from charge exchange (CX) processes in the interior region of the plasma when a neutral beam is injected. These CX neutrals well preserve information about properties of the fast ions from which neutrals originate, i.e. energy, pitch and location of the CX event, and can promptly escape from the plasma. The diagnosis of the energy spectrum of fleeing neutrals is of great importance to infer ion temperature and density, fast ion transport and wave-particle interactions. In the past decades, great effort has been paid to the development of various neutral particle analyzers (NPA). The early implementation of NPAs dates back to the 1960s [1], where incident neutrals traverse a stripping cell with helium gas for ionization and ionized neutrals are deflected by an electrostatic energy analyzer to a micro-channel plate array. Later, the ultra-thin carbon stripping foil of a few μg cm^{-2} was used to replace the stripping gas cell [2, 3]. The energy spectrometers also evolved into the $E \parallel B$ analyzer [4, 5] or time of flight analyzer [6], which are utilized not only to resolve the particle energy, but to distinguish the species of ions in the plasma. However, all of these traditional NPA systems take considerable space, limiting the accessibility of the viewing geometry and therefore the interrogated phase space. More recently, a compact solid-state NPA was developed, using fast absolute extreme ultraviolet silicon photodiode with a coated high-Z thin stripping foil of tens of nm thickness [7]. However, when operated in pulse-counting mode [7], solid-state NPAs have relatively poor temporal resolution;

when operated in current mode [8], energy resolution is lost, since the detector integrates all of the neutrals above a certain energy threshold. Ambiguities could also arise if very strong soft x-ray or ultraviolet light emission are present in the plasma. All previous systems measure currents and are therefore susceptible to noise produced by electromagnetic interference.

In this paper, we report the development of a compact scintillator-based NPA system. The system is referred to as an imaging NPA system (INPA) for the reason that it covers a broad radial range and energy range with fine resolution. The original idea is inspired by the successful implementation of phosphors as energy spectrometers in fast ion loss detectors [9] and ultra-thin carbon stripping foil suspended on fine metallic grids in space flight application [10]. The first data from INPA show excellent signal to noise and provide unprecedented phase space dynamics, demonstrating the full success of the novel NPA concept.

2. Principle and design

The principle of measurement is sketched in figure 1. As deuterium fast ions traverse an active probing neutral beam, the neutralization of the fast ions may occur through the CX process. The neutrals are not confined by magnetic fields and travel in a straight line with the energy and direction upon neutralization. Neutrals with trajectories that match the solid angle selected by the collimation arrive at stripping foils and are ionized. The incident ionized neutrals are then deflected by the Lorentz force and are dispersed onto the phosphor before completing the first period of gyro motion, as shown in figure 1. The strike position is determined by the mass and energy of the neutral, the angle between the neutral trajectory and the stripping foil plane, and the local magnetic field direction and strength. Photons are released from the phosphor depending on the property of luminescence and then collected by a fast framing charge-coupled device (CCD). Overall, the scintillator, assisted by the magnetic field inside the vacuum vessel, helps identify the energy, pitch and birth position of fleeing neutrals.

The primary goal of the INPA in the DIII-D tokamak is to study the phase space flow of energetic particles generated by multiple small amplitude Alfvén eigenmodes [11–13]. Accordingly, the INPA views the 33*lt* and 33*rt* neutral beams, shown in figure 2(*a*), and intersects from $R \sim 2.35$ m to $\sim$1.5 m at 2 cm below the midplane. This allows the system to probe the fast ion transport induced by both reversed shear Alfvén eigenmodes (RSAE) destabilized close to plasma core and toroidicity induced Alfvén eigenmodes (TAE) extending towards the plasma edge [14]. The INPA is installed at an adjacent port below the midplane and the relative angle between the sightlines and local magnetic field at the active beam results in probing of primarily passing ions having pitch $v_{\|}/v \sim 0.77$, shown in figure 2(*b*). Those particles are thought to play essential roles in the resonant interaction with Alfvén eigenmodes (AE).

In the design of the INPA, port/layout is extremely important. The following factors are taken into account to maximize

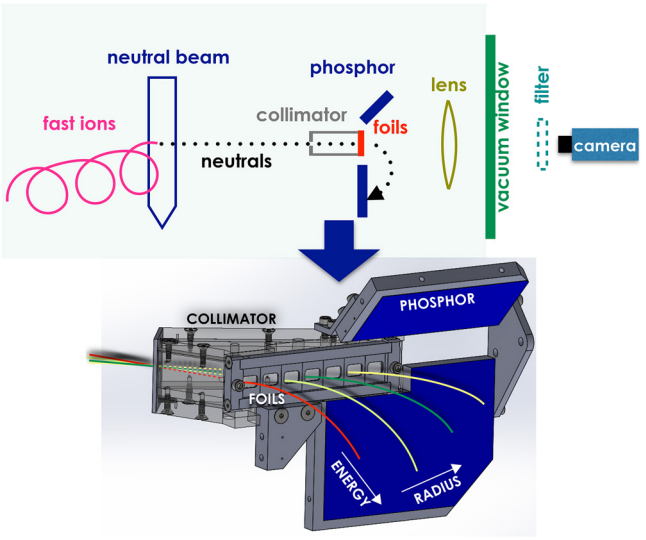

Figure 1. 2D illustration of INPA measurement principle (upper) and the 3D plot of the INPA head with particle trajectories (lower).

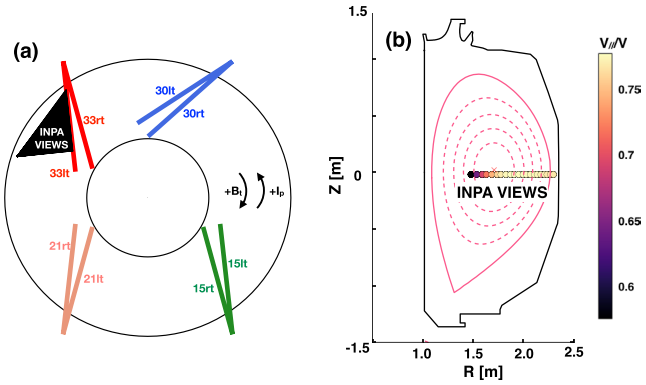

Figure 2. (*a*) The top view of INPA sightline together with the beam geometry in DIII-D tokamak, (*b*) the intersections of sightline and center of 33lt beam. INPA measured pitch is overlaid together.

the incident neutral flux: (i) the relative velocity of injected neutrals and diagnosed fast ions should match the peak of CX cross section as much as possible; (ii) the distance that the charge-exchanged fast ions travel from the neutralization spot to the carbon stripping foils should be minimized to reduce the possibility of re-ionization; (iii) the region of phase space interrogated by the INPA is well populated by the injected neutral beams. It should be emphasized that the neutral flux predicted by FIDASIM [15] using the distribution function calculated by the TRANSP NUBEAM code [16] are are well suited to this optimization problem and were used extensively in the initial INPA design process.

3. Details of hardware

Figure 3 shows that the INPA head consists of a pinhole collimator, ultra-thin carbon stripping foils, two phosphor coated substrates and a mechanical shutter. The pinhole, having a circular shape with diameter of 3 mm, is bored in the front side of the collimation box. The dimension is selected not

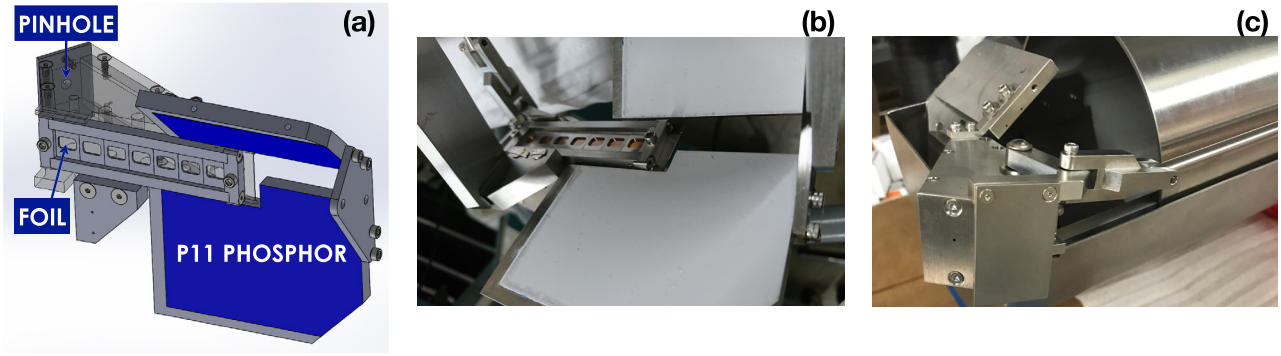

Figure 3. (*a*) CAD drawing showing the INPA collimation box, pinhole, carbon foils and phosphor substrates.The back side (*b*) and front side (*c*) views of installed INPA system.

only to provide adequate signal, but to minimize exposure of the carbon foils to electron cyclotron waves and other potential sources of degradation. Note that the pinhole dimension impacts both energy and spatial resolution.

An array of 10 nm thick, 5 mm tall, 7.3 mm wide carbon stripping foils are embedded in the back side of the collimation box, seen from figure 3(*b*). Foil survivability in the tokamak vacuum environment is the main concern, which is threatened by (i) mechanical stress from pressure differential on either side of the foils during the vacuum pumping, (ii) vibrations during the plasma disruption, (iii) temperature variation up to 150° during the wall baking, (iv) chemical and physical sputtering from cold edge neutrals. To overcome these difficulties, the foils are externally strengthened by coating onto a metallic mesh having high LPI (line per inch) of 300. An added bonus of this design is that any damage is well confined to an individual grid cell. A microscope picture of an example foil is shown in figure 4. To extend the lifetime of the stripping foils, a shutter (figure 3(*c*)) is employed which prevents sputtering from cold neutrals and potential coating from wall conditioning. Because the carbon foils are semi-transparent, a rectangle bar (not shown in figure 3) is welded on the back side of pipe behind the stripping foils to block off the optical path towards the CCD.

In traditional NPAs, the incident angle of neutrals on the stripping foil is typically nearly normal. For the INPA, however, this angle varies from 22 to 64 degrees and, as a consequence, neutrals from across the field-of-view experience a different carbon stripping foil thickness. The question arises how does this varying thickness affect the ionized flux. In previous work, it has been demonstrated that the ionization fraction of a penetrating beam, for a given energy, is independent of foil thickness (in a range representative of that used here) when it is beyond 6 atomic layers [4, 17–19], i.e. 1 nm. While the foil thickness traversed by the neutrals does not affect the ionization fraction significantly, the energy dependent emerging ionization fraction is an important effect [20], and is taken into account in the INPA modeling discussed in section 4. The net effect is a rapid increase in the ionization fraction for higher energies. Additionally, the varying thickness causes a variation in energy lost to the foil that is linear with the effective thickness and proportional to the square root of energy [4]. That is,

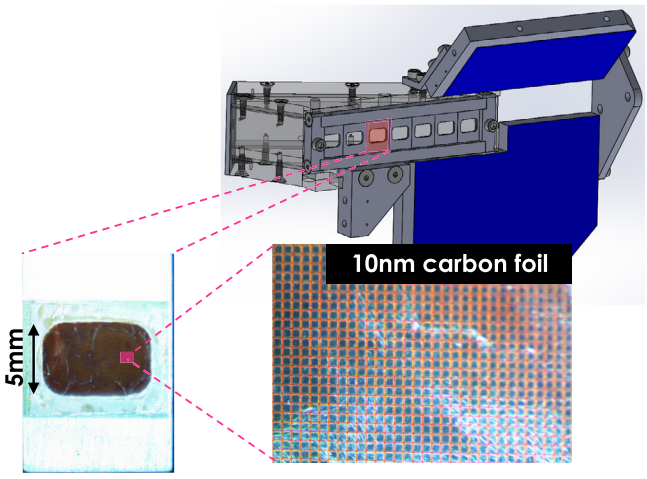

Figure 4. Microscope images of the 10 nm thick carbon foil suspended on a supporting copper mesh substrate.

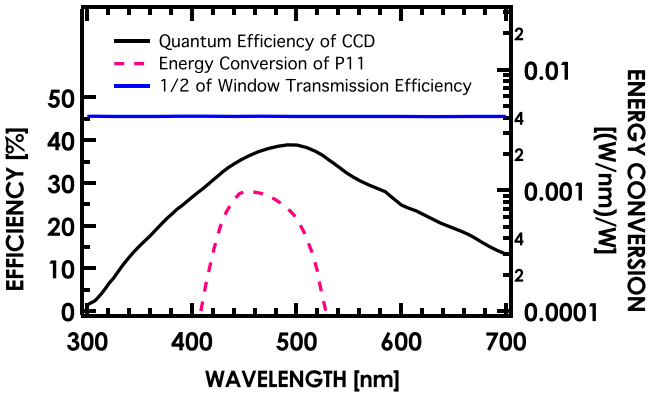

Figure 5. The quantum efficiencies of CCD and vacuum window and energy conversion of P11 phosphor as a function of wavelength.

$$\Delta E \approx 4.4 \times 10^{-2} d\sqrt{E}, \tag{1}$$

where E is the energy of incident neutrals in keV, d is the thickness of the foils in nm (taking into account the angle dependent thickness experienced by the neutrals). These effects must be considered in modeling not only the expected strike positions but the relative signals across the scintillator plane.

The phosphor ZnS:Ag (P11) is adopted for INPA, which has been successfully implemented in loss ion probes in TFTR

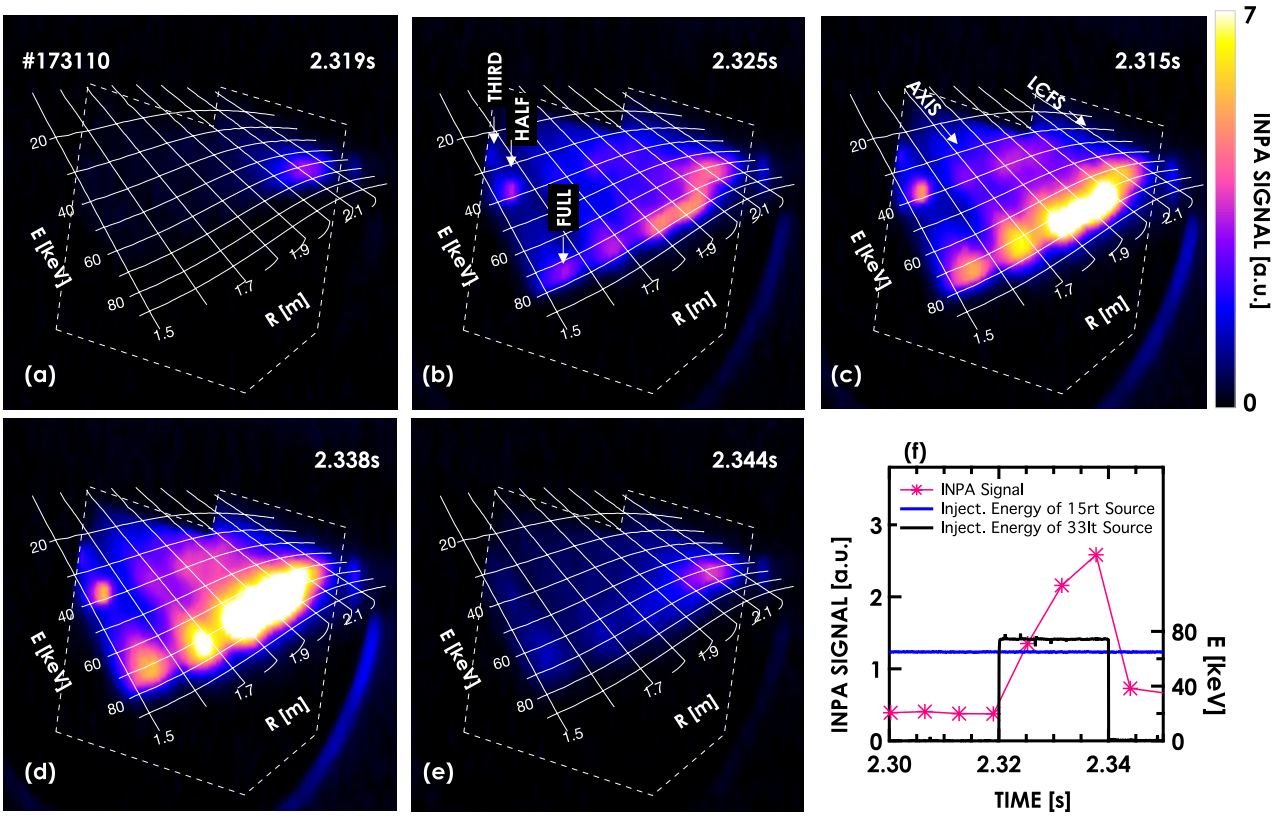

Figure 6. Series of INPA images obtained by INPA across a co-current nearly-tangential beam blip in (*a*)–(*e*) in shot 173 110. The color is scaled linearly. (*f*) The time evolution of the integrated counts over entire phosphor image and the beam voltage. The radial locations of magnetic axis and last closed flux surface (LCFS) are indicated by arrows. The dashed lines indicate the boundary of phosphor.

[21] and the Large Helical Device [22]. The phosphor has a moderate light decay time and is able to resolve fluctuations up to ∼80 kHz. The spectral sensitivity is a good match to the peak of the relative quantum efficiency of the CCD. The energy conversion efficiency of the phosphors combined with CCD quantum efficiency and window transmission spectra is illustrated in figure 5. The luminosity of the phosphor has a strong temperature dependence and the emitted light begins to diminish when the temperature exceeds a certain limit, i.e. 200 °C for P11. In DIII-D, the heat flux from the plasma raises the phosphor surface temperature up to ∼100 °C at most, much lower than the limit. To increase the diagnostic flexibility and always allow a 'blind' measurement to be made, the INPA was constructed with two separate phosphors for the two possible toroidal field orientations in DIII-D. In the standard DIII-D operational condition, ions strike the lower phosphor; for reversed toroidal field operation, ions strike the upper phosphor.

4. Verification experiment

An experiment for verifying the INPA operation is conducted in a low density of $n_e \sim 2 \times 10^{19}$ m^{-3}, nearly MHD-quiescent plasma in the DIII-D tokamak. DIII-D is equipped with eight neutral beam sources and the beam geometry is depicted in figure 2(*a*). In this experiment, the co-current nearly-tangential beam (33lt) and co-current nearly-perpendicular beam source (33rt) inject for 20 ms in turn as active beams. Meanwhile, a co-current nearly-perpendicular beam (15rt) out of the INPA view stays constant. The injection energy of the active beams and 15rt beam differs: the active sources are injected at 75 keV and the other one is at 65 keV, as shown in figure 6(*f*).

The interpretation of the INPA images relies on the energy and spatial grid calculated from forward modeling using the real geometry. The computation process is summarized as follows. The neutral trajectory is treated as a straight line from the plasma to stripping foils through the pinhole. The neutral-foil interaction is simulated by considering the energy loss, as given in equation (1). Small angular scattering by the foils is neglected. The gyro-orbit of ionized neutrals is then followed until they strike the phosphor plane. The grid, i.e. contours of incident neutral energy and radius probed in the plasma, together with relevant images, are illustrated in figures 6(*a*)–(*e*) .

The sequence of INPA images with overlaid energy and radius grids clearly show the local fast ion phase space evolution throughout short blips of the active beam sources and confirm the diagnostic functionality:

(i) The INPA image series across a blip of nearly-tangential active source, i.e. 33lt beam, is illustrated in figures 6(*a*)–(*e*). The figures 6(*a*) and (*e*) are images when the active source is off. The signal comes from the CX reaction between the fast ions traveling in plasma peripheral region and cold edge neutrals, called the 'passive' signal. Conversely, figures 6(*b*)–(*d*) are images when the active source is on. In these images, the passive signal is still

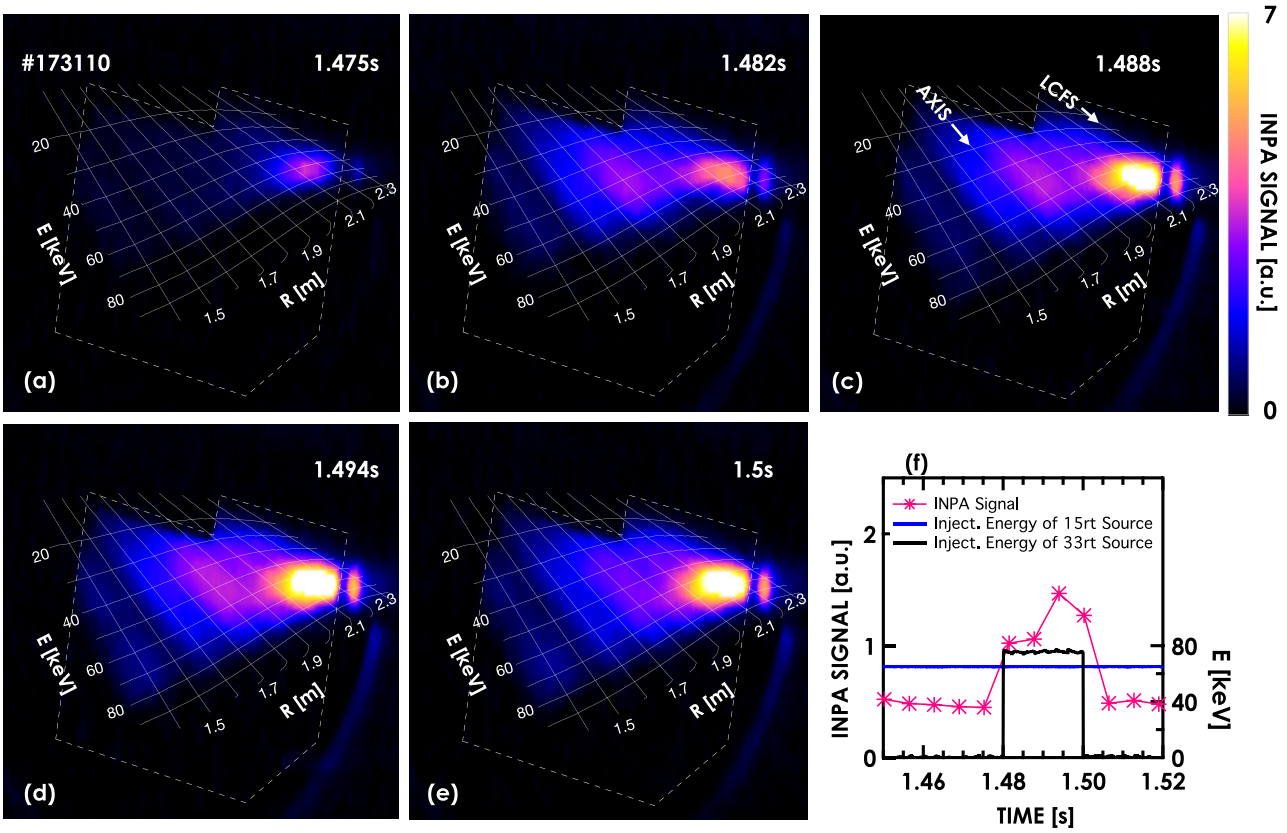

Figure 7. The image series obtained by the INPA across a co-current nearly-perpendicular beam blip in (*a*)–(*e*) in shot 173 110. The color is scaled linearly. (*f*) The time evolutions of the integrated counts over the whole image and the beam voltage. The radial locations of magnetic axis and LCFS are indicated by arrows. The dashed lines indicate the boundary of phosphor.

present but the dominant signal is due to the CX reaction between the fast ions traveling in the plasma and beam neutrals, called the 'active signal'. The band structures in the images of figure 6, following the contours at constant major radius, are produced by the stainless steel structure for supporting each foils shown in figure 4. In figure 6(*b*), the neutral flux extends up to 75 keV, which is the injection energy of the probe beam, and spans all radii.

(ii) The neutral flux at the maximum energy continuously increases when the 33lt beam stays on, as shown in figures 6(*c*) and (*d*). It is also recognized from the image series that fast ions start to slow down away from the injection energy and fill in the phase space below ∼75 keV. Moreover, the full, half, and one third energy components of the neutral beam are all distinguishable, indicated by the arrows in figure 6(*b*) as one example. Interestingly, the slowing towards lower energy is not as clear for the half-energy component as for the full energy component. This is due to the significant pitch angle scattering of fast ions with half energy of 37.5 keV close to or lower than the critical beam energy E_c, which, for instance, at the plasma core is ∼37.3 keV for $T_e \sim 2$ keV. However, this effect is less signifiant on those particles with the full energy of 75 keV, which is much larger than E_c.

(iii) The INPA image series across a blip of the nearly-perpendicular active source (33rt), illustrated in figures 7(*a*)–(*e*), exhibits very different characteristics. First, though the injection energy is the same as the nearly-tangential source at 75 keV, the upper bound of the measured neutral energy in the plasma core is obviously lower than the injection energy. For instance, taking the energy resolution of ∼7.5 keV into consideration, the maximum energy sits at ∼61 keV at $R \sim 1.86$ m in figure 7(*d*). The deviation away from injection energy is smaller in the chords viewing the plasma edge region. The other difference is that the signal level using the nearly-perpendicular beam as a probe source is much lower than the signal using nearly-tangential source. Moreover, the slowing-down process from the observed maximum energy is not discernible from the image series in this case.

All of the above differences are to be expected and result from a combination of the varied pitch deposited by the different beams, the INPA interrogated pitch and the effects of pitch angle scattering. As shown in figure 8, a nearly-perpendicular source populates the trapped particles on the low field side and passing particles having pitch up to ∼0.62 in the high field side. Nevertheless, none of them can directly populate fast ions into the INPA interrogated phase space with pitch of ∼0.77 on the low field side, given as plus symbol in figure 8. That is, the phase space diffusion through pitch angle scattering is essential for the INPA to detect the contribution from nearly-perpendicular beams. On the contrary, the nearly-

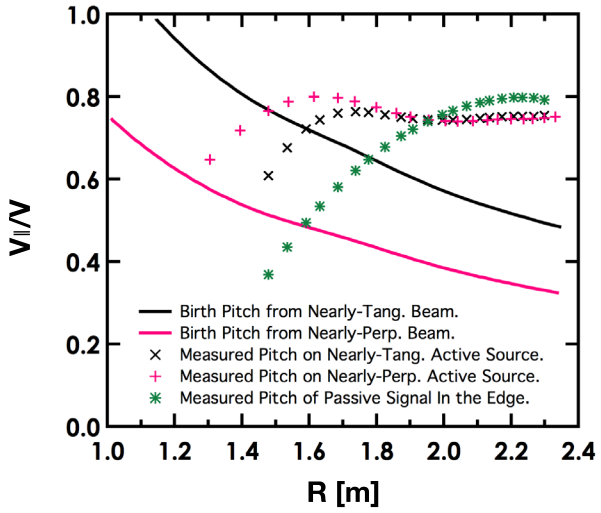

Figure 8. The birth pitch of fast ions populated by nearly-tangential beam (black line) and the nearly-perpendicular beam (red line) and the interrogated pitch by the INPA when using the nearly-tangential beam 33lt as the active beam (black crosses), using the nearly-perpendicular beam as active beam (red plus). The probed pitch of the passive signal (green asterisk). Note, all passive signal originates from the edge but is plotted at the equivalent phosphor position corresponding to the intersection radii between the sightline and the center of the 33lt beam.

tangential beam populates the passing ions up to a pitch of 1.0 on the high field side. That is, after an excursion to the low field side, the fast ions can be immediately detected by the INPA without experiencing any pitch angle scattering or energy slowing-down.

A simple comparison with theory, using the deflection time τ_d, which measures the rate at which the particle is scattered into the perpendicular direction to its initial velocity, and slowing-down time τ_s, which measures the amount of time that the energy of fast ions decays by a factor of $1/e$, supports the above interpretation. For electron temperature of 2.78 keV and density of 3.25×10^{19} m^{-3} at $R \sim 1.86$ m measured by the Thomson Scattering system, ion temperature assumed to be the same as the electron temperature, the τ_d and τ_s at $t = 1500$ ms are estimated to be ~190 ms and ~71 ms, respectively. The difference from the pitch populated by nearly-perpendicular neutral beam to the pitch interrogated by the INPA is ~0.33, i.e. from ~0.42 to ~0.75, corresponding to the deflection angle of $\delta\theta \sim 24°$. The equation $\delta t = (\delta\theta/90)^2\tau_d$ suggests that it takes $\delta t \sim 13.6$ ms to scatter the fast ions populated by nearly-perpendicular beam, i.e. 33rt beam, into the phase space interrogated by the INPA. As a consequence, the upper bound of fast ion energy decreases from the injection energy of $E_0 = 75$ keV to ~62 keV, following the relation:

$$E = E_0 \exp(-\delta t/\tau_s). \quad (2)$$

This estimate matches the observed maximum energy of neutral flux at ~61 keV.

The consistency of estimated δt with the measurements is also reflected in the evolution of maximum energy of neutral flux revealed in the INPA image series: the image of figure 7(*b*) is obtained immediately after the switch-on of the active source. Since the elapsed time from the beam switch-on is much shorter than the δt, the measured image is dominated by the confined distribution function of the beam ions previously injected by the continuous 15rt beam at 65 kV (also a nearly-perpendicular beam). After a duration of 12 ms, a jump-up of INPA signal is observed at 1.493 s (see figure 7(*f*)). More importantly, the maximum energy of neutral flux in the plasma core clearly increases by ~10 keV, as seen from figures 7(*b*) and (*d*). Since the injection energy of 15rt source and 33rt source differs by ~10 keV, as shown in figure 7(*f*), these facts indicate that the fast ions populated by 33rt beam take roughly a duration of ~12 ms to enter the phase space interrogated by the INPA through pitch angle scattering. This roughly agrees well with the estimated $\delta t \sim 13.6$ ms.

It also should be pointed out that, for the similar reasons, as seen from figures 6 and 7, the 'passive' signal contributed by the constant injection of nearly-perpendicular beam centers at ~55 keV, which is also lower than the injection energy of 65 keV.

(iv) Figures 6(*e*) and 7(*e*) shows that the chords viewing the neutral beam source near the plasma edge have a large passive signal. This is because the integrated neutral density along the sightlines viewing the neutral beam source near the plasma edge is much higher than those chords viewing the the neutral beam source near the core.

(v) Preliminary results of the simulated INPA images in figures 9(*b*) and (*d*) are compared with the experimental ones in figures 9(*a*) and (*c*). Many of the important features of the experimental data, such as striking positions on the phosphor for a given probed radius and energy, slowing down process of the fast ions, rate at which fast ions are populated, etc. are reproduced by the simulations. The procedure of the simulation is as follows. First, the classical fast ion distribution function is calculated by the TRANSP NUBEAM code [16], using the measured electron temperature and density profiles. Then, neutral flux towards the INPA stripping foils is estimated by FIDASIM [15], taking into account the actual INPA gemoetry, CX reaction and attenuation as neutrals travel. As a final step, another code (INPASIM) simulates the neutral-foil interaction including energy dependent ionization efficiency and energy loss of particles to the foils, and finally traces the ionized neutral's Lorentz motion to the strike position on the INPA phosphor. At present, the intensity of light emission from the P11 phosphor is crudely assumed to be linearly proportional to the energy of incident ions. Moreover, the passive signal contributed by the probing beam (33lt) is not included in the modeling. The above two effects would be responsible for the deviation between

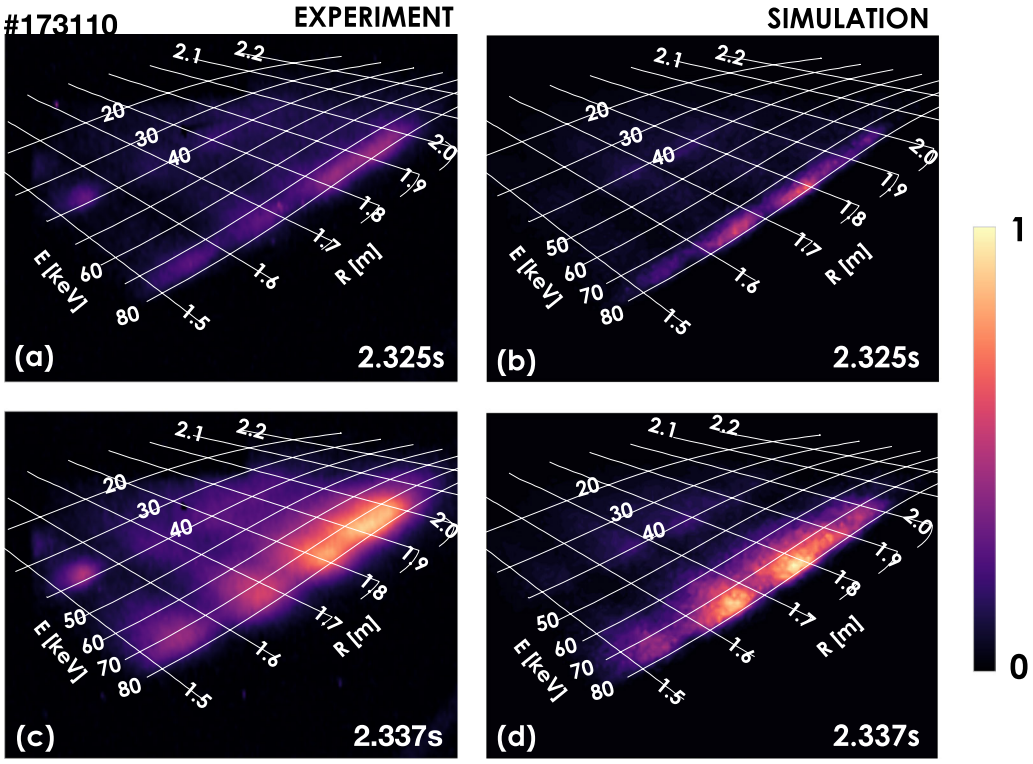

Figure 9. INPA images obtained at ∼2.325 s (*a*) and ∼2.337 s (*c*) in shot 173 110 and corresponding modeled images given in (*b*) and (*d*). The color is scaled linearly. The passive signal is linearly interpolated using the image before and after the beam blip in figure 6(*f*) and subtracted from the measured images.

the experimental images and the synthetic ones. Note that the passive contribution from the nearly perpendicular beam (15rt), estimated by linear interpolation of the images obtained before and after the beam blip, is subtracted in figures 9(*a*) and (*c*).

Reversing the toroidal field direction is another test which has been employed to validate the INPA operation. An image comparison between normal B_t and reverse B_t is given in figure 10. As expected, the image emerges in the upper phosphor instead of the lower one after B_t is reversed.

The signal to noise ratio (SNR) of the INPA is exceptionally good. The primary source of noise comes from gamma rays accidentally captured by the CCD camera. This means the SNR can be further improved by adding shielding to reduce the radiation levels at the camera. The energy resolution suggested by the modeling and experimental data is ∼7.5 keV. The spatial resolution is ∼15% of normalized minor radius in the low field side, i.e. ∼7 cm in the midplane, and the pitch angle resolution is ∼5°, determined by the finite width and height of the active neutral beam along with the INPA aperture sizes.

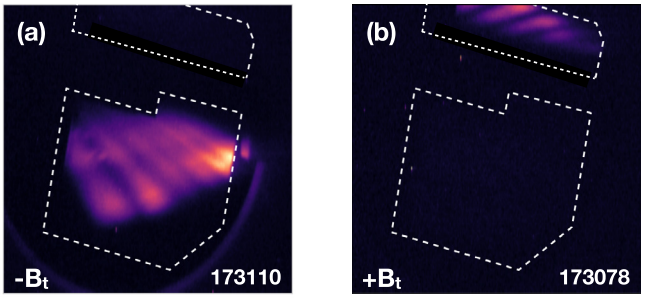

Figure 10. INPA images obtained in (*a*) normal B_t and (*b*) reverse B_t. The dotted lines indicate the boundary of the phosphors substrates.

5. 'Snapshot' of fast ion redistribution observed by INPA

MHD events like fast ion driven kink modes [23], fast ion driven interchange modes [24–26], sawteeth [27], etc can cause a sudden and rapid transport of energetic particles from the core that the INPA is capable of probing. As one example, severe fast ion redistribution induced by a moderate sawtooth crash is clearly resolved and is shown in figure 11. The differential image, i.e. subtraction of the image at 3.972 s before the sawtooth from the image at 3.978 s after the sawtooth, shows a large decrease of incident neutral flux inside the $q = 1$ rational surface, i.e. from 1.65 m to 1.885 m, accompanied by a correspondingly large increase at larger radii outside the $q = 1$ surface. The density perturbation in the very edge region by the sawtooth is ∼5%. Note that the increase of INPA signal around the last closed flux surface (LCFS) at ∼2.1 m is not noticeable, indicating that passing fast ions are redistributed instead of the loss from plasma.

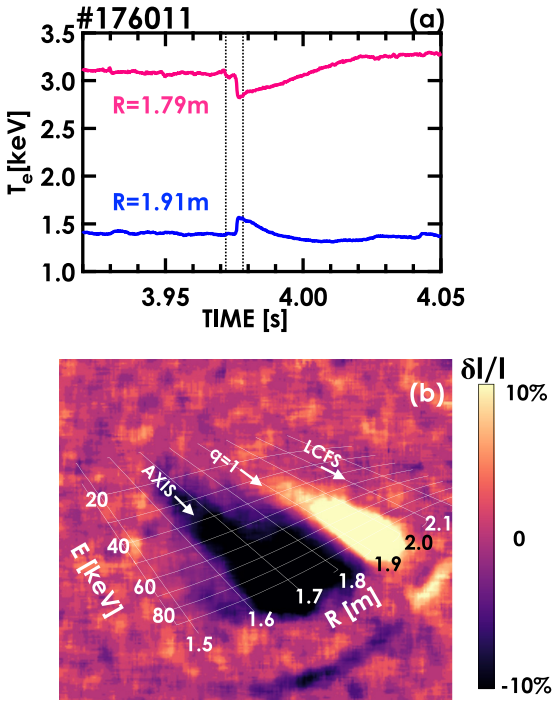

Figure 11. (*a*) Sawtooth crash indicated by time evolution of electron temperature inside and outside $q = 1$ rational surface, measured by electron cyclotron emission. (*b*) Image difference between INPA signal obtained at $t = 3.978$ s and $t = 3.972$ s, which two time slices are before and after the sawtooth crash, as shown as vertical line in (*a*), respectively. The energy and radius grids are overlaid.

6. Summary

An INPA has been successfully built and experimentally verified in the DIII-D tokamak. The diagnostic is able to resolve a broad region of confined fast ion phase space with excellent energy and spatial resolution at well defined pitch angles. Measurements of individual active beam blips clearly show the full, half and third energy components, spatial distribution, slowing down process and pitch angle scattering process. Also, as part of the verification process, operation with reversed toroidal field shows the expected behavior. A clear redistribution of confined fast ions by a sawtooth crash is given as one example, demonstrating the great potential of the INPA to studies of the phase space dynamics induced by various MHD events. It should be emphasized that, for the study of AE modes, in theory, magnetic moment μ would be conserved during the resonant interaction between AE waves and fast ions, when the frequency of AE modes is much lower than the cyclotron frequency of fast ions [28], i.e. $\omega_{AE} \ll \omega_{ci}$. The current design of the INPA covers a broad range of the phase space with nearly constant μ at the energy of interest, i.e. above 60 keV. This feature benefits the study of the fast ion flow in phase space induced by multiple small amplitude AE modes in conserved μ space.

Combined with modeling, the INPA may also be useful to infer the edge neutral density in the plasma peripheral region from the ratio of active to passive signal, which will be investigated in the future. The ability of the INPA to measure the distribution of fusion products by rotating the phosphor plane to almost vertical against the stripping foil plane and/or using thick stripping foils for the reduction of incident tritium and helium energy, will also be investigated.

Acknowledgment

The authors would like to thank Luke Stagner for fruitful discussions on FIDASIM [15] calculation and also would like to thank DIII-D technical staff for their great effort in the INPA installation. This work was supported by US DOE Contract DE-FC02-04ER54698.

References

[1] Afrosimov V.V. and Glakkovskii I.P. 1967 *Sov. Phys. Tech. Phys.* **12** 1135
[2] Gottand Y.V. and Tel'kovskii V.G. 1965 *Sov. Phys. Tech. Phys.* **9** 1628
[3] Gottand Y.V. and Motlich A.G. 1978 *Nucl. Instrum. Methods* **155** 443
[4] Beiersdorfer P., Roquemore A.L. and Kaita R. 1987 *Rev. Sci. Instrum.* **58** 2092
[5] Carolipio E.M. and Heidbrink W.W. 1997 *Rev. Sci. Instrum.* **68** 304
[6] Bracco G., Betello G., Mantovani S., Moleti A., Tilia B. and Zanza V. 1992 *Rev. Sci. Instrum.* **63** 5696
[7] Shinohara K., Darrow D.S., Roquemore A.L., Medley S.S. and Cecil F.E. 2004 *Rev. Sci. Instrum.* **75** 3640
[8] Zhu Y.B., Bortolon A., Heidbrink W.W., Celle S.L. and Roquemore A.L. 2012 *Rev. Sci. Instrum.* **83** 10D304
[9] Zweben S.J., Boivin R.L., Diesso M., Hayes S., Hendel H.W., Park H. and Strachan J.D. 1990 *Nucl. Fusion* **30** 1551
[10] McComas D.J., Allegrini F., Pollock C.J., Funsten H.O., Ritzau S. and Gloeckler G. 2004 *Rev. Sci. Instrum.* **75** 4863
[11] Collins C.S. *et al* 2016 *Phys. Rev. Lett.* **116** 095001
[12] Heidbrink W.W. *et al* 2017 *Phys. Plasma* **24** 056109
[13] Collins C.S. *et al* 2017 *Nucl. Fusion* **57** 086005
[14] Van Zeeland M.A., Kramer G.J., Austin M.E., Boivin R.L., Heidbrink W.W., Makowski M.A., McKee G.R., Nazikian R., Solomon W.M. and Wang G. 2006 *Phys. Rev. Lett.* **97** 135001
[15] Heidbrink W.W., Liu D., Luo Y., Ruskov E. and Geiger B. 2011 *Commun. Comput. Phys.* **10** 716
[16] Pankin A., Mccune D., Andre R., Bateman G. and Kritz A. 2004 *Comput. Phys. Commun.* **159** 157
[17] Hall T. 1950 *Phys. Rev.* **79** 504
[18] Phillips J.A. 1955 *Phys. Rev.* **97** 404
[19] Kreussler S. and Sizmann R. 1982 *Phys. Rev.* B **26** 520
[20] Gonin M., Kallenbach F.L. and Bochsler P. 1993 *Rev. Sci. Instrum.* **65** 648
[21] Zweben S.J. *et al* 1995 *Nucl. Fusion* **35** 893
[22] Ogawa K., Isobe M., Toi K., Spong D.A., Osakabe M. and LHD Experiment Group 2012 *Nucl. Fusion* **52** 094013
[23] McGuire K. *et al* 1983 *Phys. Rev. Lett.* **50** 891
[24] Du X.D. *et al* 2015 *Phys. Rev. Lett.* **114** 155003
[25] Du X.D. *et al* 2016 *Nucl. Fusion* **56** 016002
[26] Du X.D. *et al* 2017 *Phys. Rev. Lett* **118** 125001
[27] Goeler V. *et al* 1974 *Phys. Rev. Lett.* **33** 1201
[28] Chen L., Vaclavik J. and Hammett G.W. 1988 *Nucl. Fusion* **28** 389